

Co Doped Zinc Oxide Nanoparticles: Synthesis, Characterization and Selective In Vitro Cytotoxicity

K. Vasuki, Dr.R.Manimekalai

Department of Chemistry, Kongunadu Arts and Science College, Coimbatore, Tamil nadu, India.

Date Of Submission: 01-05-2021

Date Of Acceptance: 10-05-2021

ABSTRACT : Cobalt doped ZnO nanoparticles have been synthesized by thermal decomposition of Cobalt doped zinc laurate hydrazinate precursor. The precursor prepared by coprecipitation method is characterized by analytical, ICP-AES, infrared (IR), thermogravimetric (TG), and differential thermal analysis (DTA). Using appropriate heat treatment the precursor undergoes self-propagating auto combustion to give Co doped ZnO nanoparticles. These are characterized using IR, Energy-dispersive X-ray spectroscopy (EDS), X-ray diffraction (XRD), Scanning electron microscope (SEM), UV-Visible-NIR and Transmission electron microscope (TEM). From the X-Ray diffraction patterns, the crystallite size of the metal oxide particles is estimated. The morphology of the nanoparticles is studied using SEM analysis. The in vitro cytotoxicity and the reactive oxygen species generation of the nanoparticles against human breast cancer cells (MCF-7) and the human embryonic kidney cells (HEK 293) by MTT assay are studied.

Keywords: Nanoparticles Zinc oxide, In vitro cytotoxicity, Reactive oxygen species.

I. INTRODUCTION

Inorganic nanoparticles are promising materials for applications in medicine, such as cell imaging, biosensing, drug delivery, and cancer therapy. Among inorganic materials, metal oxide nanoparticles are of special interest as they can participate in cellular redox reactions and have photocatalytic activity [1]. Zinc oxide NPs show strong inherent cytotoxicity to kill cancerous cells compared to normal cells [2,3]. Generation of reactive oxygen species (ROS) is believed to be a major mechanism of cytotoxicity [4]. ZnO exhibits unique opto-electronic properties, non-toxicity, and high thermal and chemical stability. The wide band gap of ZnO limits its light absorption at the near ultra-violet region. [5]. The absorbing spectral region can be shifted or extended to visible region through suitable addition of impurities (doping). If zinc oxide is made to absorb in visible region it can

produce reactive oxygen species when irradiated with visible light, which can be used to kill cancer cells, instead of dangerous UV light [6]. In trace amount zinc and cobalt are essential elements for human and animal health and additionally they are photocatalytic materials. Also, doping with transition metals like Co improves the optical properties of ZnO by hindering the recombination of electron hole pair generated from optical absorption [7, 8]. The ionic and covalent radius of cobalt Co (0.072 nm and 0.116 nm) matches with that of Zn (0.074 nm and 0.125 nm), and its divalent state ensures a high solubility in ZnO matrix [9]. So it can be doped properly into the lattice without causing any change in the crystal structure of ZnO. Recently, many studies on Co doped zinc oxide nanomaterials have been reported. Most of those studies were primarily focused on optical, electrical, and magnetic properties of Co-doped ZnO nanoparticles [10]. There are only few reports on the antimicrobial and anticancer activities of Co-doped ZnO nanoparticles.

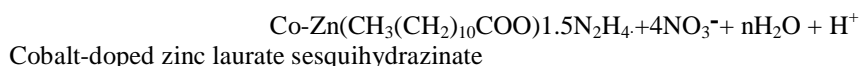
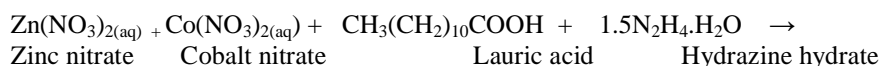
Thermal decomposition of precursor metal hydrazine carboxylate has been used to prepare nanoparticles of zinc oxide [11], cuprites [12], ferrites [13],cobaltites [14]. These precursors once ignited decompose in the presence air with the evolution of N₂, H₂ and CO₂ to yield oxide nanoparticles. The synthesis is inexpensive and yields high purity products compared to various chemical methods such as sol-gel, spray-dry which are used to prepare nanoparticles. Here we present the preparation, characterization, optical properties and the cytotoxic response of Co-doped zinc oxide nanoparticles in human breast cancer (MCF-7) cells and the human embryonic kidney normal cells (HEK 293).

II. EXPERIMENTAL SECTION

2.1.1 Preparation of the Precursor Cobalt-doped Zinc laurate hydrazinate Co-Zn(Lau)1.5N₂H₄

The precursor was prepared by coprecipitation method. The ethanolic solution (50 mL) of lauric acid (1.020 g, 0.0051 mol) was stirred with 99–100% pure hydrazine hydrate (4 mL, 0.008 mol). To this, a freshly prepared aqueous mixture (50 mL) of zinc nitrate

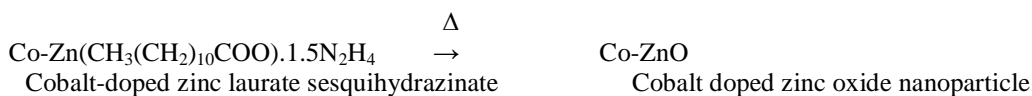
hexahydrate (1.37 g, 0.0046 mol) and cobalt nitrate hexahydrate (0.1 g, 0.0005 mol) was added dropwise with constant stirring. The precursor formed immediately, was kept aside for an hour for digestion, filtered, washed with water and alcohol followed by diethylether and air-dried.



2.1.2 Preparation of Co-ZnO nanoparticles

Thermal decomposition of the precursor led to the formation of oxide nanoparticles. The dried precursor was transferred to silica crucible and heated to red hot condition in an ordinary atmosphere. The precursor got ignited, underwent

autocatalytic decomposition using atmospheric oxygen resulting in the formation of fine oxide products. The obtained nanoparticles were further heated at 400°C to remove any residual carbon formed during the decomposition



Cobalt doped ZnO nanoparticle prepared, hereafter referred to as Co-ZnO NPs.

2.2 Quantitative Methods

The hydrazine content in the precursor was chemically determined volumetrically using 0.025 M KIO₃ as titrant under Andrew's condition. Elemental analysis of C, H and N were performed on a Elementar Vario EL III analyzer. Actual doping concentration was quantified with inductively coupled plasma atomic emission spectroscopy (ICP-AES) using Thermo Electron IRIS INTREPID II XSP DUO Flexible axial and radial view instrument, with high concentration capabilities, after digesting the precursor in HNO₃, made to 50ml, filtered and analysed.

alumina as reference. The temperature range was ambient to 700 °C. XRD pattern was recorded using Bruker AXS D8 Advance X-ray diffractometer using CuK_α radiation (1.5406 Å) at 40 kV and 40 mA. Scanning electron microscopy (SEM) was performed with a JEOL Model JSM - 6390LV microscope. The morphology of the synthesized NPs was characterized using transmission electron microscopy (TEM) Jeol/JEM 2100 model operating with an accelerating voltage of 200 kV. UV-Vis-NIR absorption spectra was recorded at room temperature on Perkin Elmer lambda 950 UV-VIS-NIR instrument with spectral range of 175-3300 nm having Deuterium lamp (UV region) and Tungsten- Halogen lamp (VIS-NIR region) as source, PMT (UV-VIS) and Peltier cooled PbS (NIR) as Detectors.

2.3 Sample characterization

All reagents for the synthesis were obtained commercially and used as received. The infrared spectrum of the solid precursor sample was recorded using KBr pellets in the range of 4000–400 cm⁻¹ on Thermo Nicolet, Avatar 370-FT-IR spectrometer. EDX energy-dispersive X-ray spectroscopy was performed by SIGMA HV – Carl Zeiss with Bruker Quantax 200 – Z10 EDS Detector. The simultaneous TG-DTA experiment was carried out in Perkin Elmer, Diamond TG/DTA thermal analyzers. Thermal analysis was carried out in nitrogen atmosphere at the heating rate of 10°C per minute using 4.365mg of the sample. Platinum cups were used as sample holders and

2.4 In Vitro Cytotoxicity

2.4.1 Cell lines and cell culture.

The human breast adenocarcinoma cell line (MCF7) was obtained from National Centre for Cell Science (NCCS), Pune and grown in Eagles Minimum Essential Medium containing 10% fetal bovine serum (FBS). The cells were maintained at 37°C, 5% CO₂, 95% air and 100% relative humidity. Maintenance cultures were passaged weekly, and the culture medium was changed twice a week. The human embryonic kidney cell line

(HEK 293) was obtained from National Centre for Cell Science (NCCS), Pune and grown in Eagles Minimum Essential Medium containing 10% fetal bovine serum (FBS). The cells were maintained at 37°C 5% CO₂, 95% air and 100% relative humidity. Maintenance cultures were passaged weekly, and the culture medium was changed twice a week.

2.4.2 Estimation of cytotoxicity: cell treatment procedure

The monolayer cells were detached with trypsin-ethylenediaminetetraacetic acid (EDTA) to make single cell suspensions and viable cells were counted using a hemocytometer and diluted with medium containing 5% FBS to give final density of 1x10⁵ cells/ml. One hundred microlitres per well of cell suspension were seeded into 96-well plates at plating density of 10,000 cells/well and incubated to allow for cell attachment at 37°C, 5% CO₂, 95% air and 100% relative humidity. After 24h the cells were treated with serial concentrations of the test samples. They were initially dispersed by sonication in phosphate buffered saline (PBS) and an aliquot of the sample solution was diluted to twice the desired final maximum test concentration with serum free medium. Additional four serial dilutions were made to provide a total of five sample concentrations. Aliquots of 100 µl of these different sample dilutions were added to the appropriate wells already containing 100 µl of medium, resulting in the required final sample concentrations. Following sample addition, the plates were incubated for an additional 48 h at 37°C, 5% CO₂, 95% air and 100% relative humidity. The medium without samples were served as control and triplicate was maintained for all concentrations.

2.4.3 MTT assay

[4,5-dimethylthiazol-2-yl]2,5-diphenyltetrazolium bromide (MTT) is a yellow water soluble tetrazolium salt. A mitochondrial enzyme in living cells, succinate-dehydrogenase, cleaves the tetrazolium ring, converting the MTT to an insoluble purple formazan. Therefore, the amount of formazan produced is directly

proportional to the number of viable cells. After 48 h of incubation, 15µl of MTT (5mg/ml) in phosphate buffered saline (PBS) was added to each well and incubated at 37°C for 4h. The medium with MTT was then flicked off and the formed formazan crystals were solubilized in 100µl of DMSO and then measured the absorbance at 570 nm using micro plate reader. The % cell inhibition was determined using the following formula. % Cell Inhibition = 100- {Abs (sample)/Abs (control) x100}. Nonlinear regression graph was plotted between % Cell inhibition and Log concentration and IC₅₀ was determined using Graph Pad Prism software.

2.4.4. Reactive Oxygen Species (ROS)

Assay. 2',7'-Dichlorodihydrofluorescein diacetate (H2DCFDA) is a cell permeable molecule that gets cleaved in the presence of intracellular ROS to generate a highly fluorescent 2',7'-dichlorofluorescein molecule. The ROS levels induced in cells upon nanoparticle treatment were evaluated using flow cytometry (BD FACS Aria, USA). Cancer and normal cells were seeded into 6-well plates at a density of 10⁵ cells per well and incubated for 24 h. Old media was removed and the cells were treated with media containing varying concentrations of nanoparticles. Cells treated with media alone served as negative control. Following treatment for 12 h and a wash with PBS, the cells were treated with 10 mM H2DCFDA. Post incubation of the cells for 30 min, they were washed with PBS and trypsinized. The cells suspended in PBS were analyzed using flow cytometry. Fluorescence intensity was recorded by excitation at 485 nm, and emission at 535 nm using multiwell micro plate reader

III. RESULTS AND DISCUSSION

3.1 Characterization of the precursor Co-Zn(Lau).1.5N₂H₄

3.1.1 Energy Dispersive X-ray Analysis (EDX)

EDX analysis shown in Figure 1 shows the presence of metals, carbon, nitrogen and oxygen in the the precursor, which confirmed that the precursor contains only carboxylate group (laurate), hydrazine, metals and no other impurities.

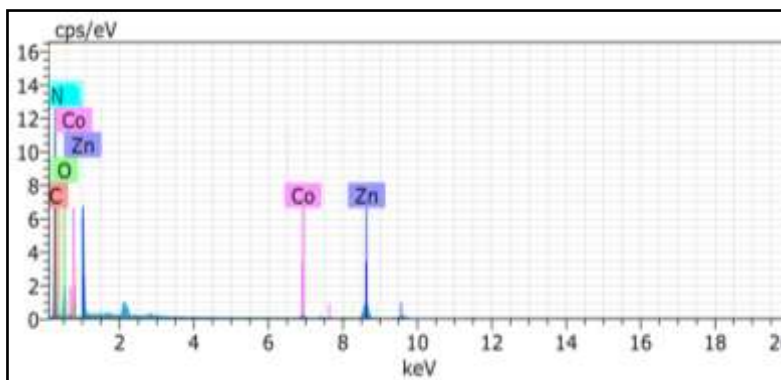


Figure 1 EDS of Co-Zn(Lau).1.5N₂H₄

3.1.2. Chemical analysis

The percentage of metals, hydrazine, carbon, nitrogen and hydrogen in the precursors were analysed and given in Table 1 The percentage of hydrazine in the precursor was determined by

titration using KIO₃ as the titrant, by volumetric analysis under Andrew's condition [15]. The metal and elemental compositions of the precursor were analysed using ICP-AES and CHN analyser respectively

Table 1 Chemical analysis of Co-Zn(Lau).1.5N₂H₄

Hydrazine %		Elemental analysis %						Metal %			
		Carbon		Hydrogen		Nitrogen		Zn		Co	
obs	cal	obs	cal	obs	cal	obs	cal	obs	cal	obs	cal
14.15	13.90	41.10	42.72	8.10	8.60	11.95	12.46	25.80	26.57	1.18	1.67

Lau = (CH₃(CH₂)₁₀COO⁻) Obs=observed value, cal =calculated value

3.1.3 Thermal Analysis

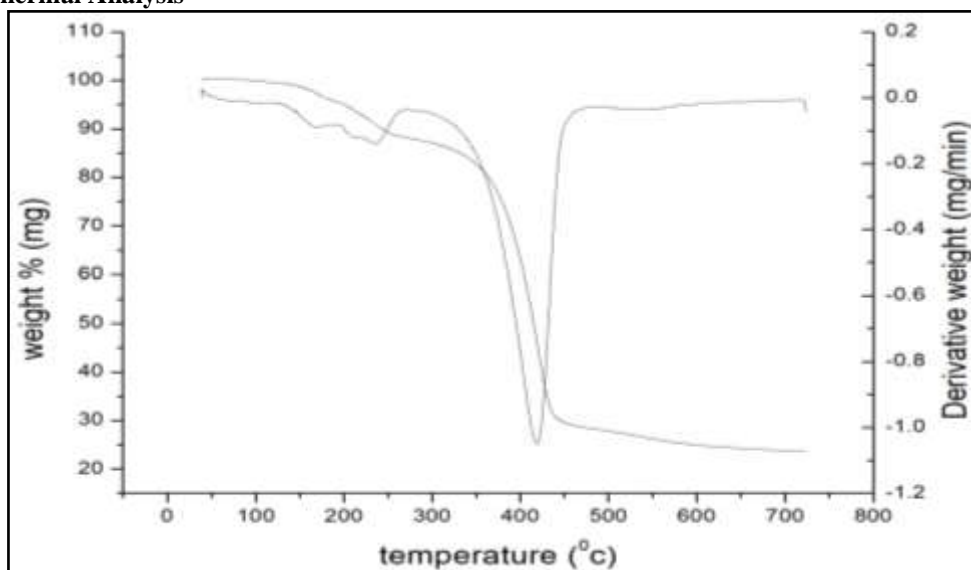


Figure 2 TG-DTA curve of Co-Zn(Lau).1.5N₂H₄

Table 2 Thermal analysis of Co-Zn(Lau).1.5N₂H₄

Precursor	TG temp range °C	Mass loss %	DTA Peak temp °C	Decomposition
Co-Zn(Lau).1.5N ₂ H ₄	150-255	13%	168 (+) 235 (+)	Co-Zn(Lau)
M.Wt :371 g/mol	300-450	59%	419 (+)	Co-ZnO

Lau=(CH₃(CH₂)₁₀COO⁻) (+): endotherm

As can be observed from Figure 2, the precursor loses weight in two steps. From TG curve the first step is the loss of hydrazine at a temperature range between 150°C and 225°C with the observed weight loss of 13%. The corresponding peak in DTA curve is observed as two overlapping endotherm peak at 168°C and 235°C. The major weight loss of 59% on the TG curve from 300°C to 450°C is attributed to the second step involving decarboxylation of the precursor. This is indicated by a sharp endothermic

peak in DTA curve at 419°C which gives Co-ZnO as the final residue, which is stable over 700°C without any further weight loss. The thermal analysis data are given in Table 2.

The analytical data of the precursor obtained from chemical (Table 1) and thermal (Table 2) analysis are found to be in good agreement with the values calculated, considering the molecular stoichiometric composition as Co_{0.1}Zn(C₁₂H₂₄O₂).1.5N₂H₄ for precursor Cobalt doped Zinc laurate hydrazinate.

3.1.4 FT-IR Analysis

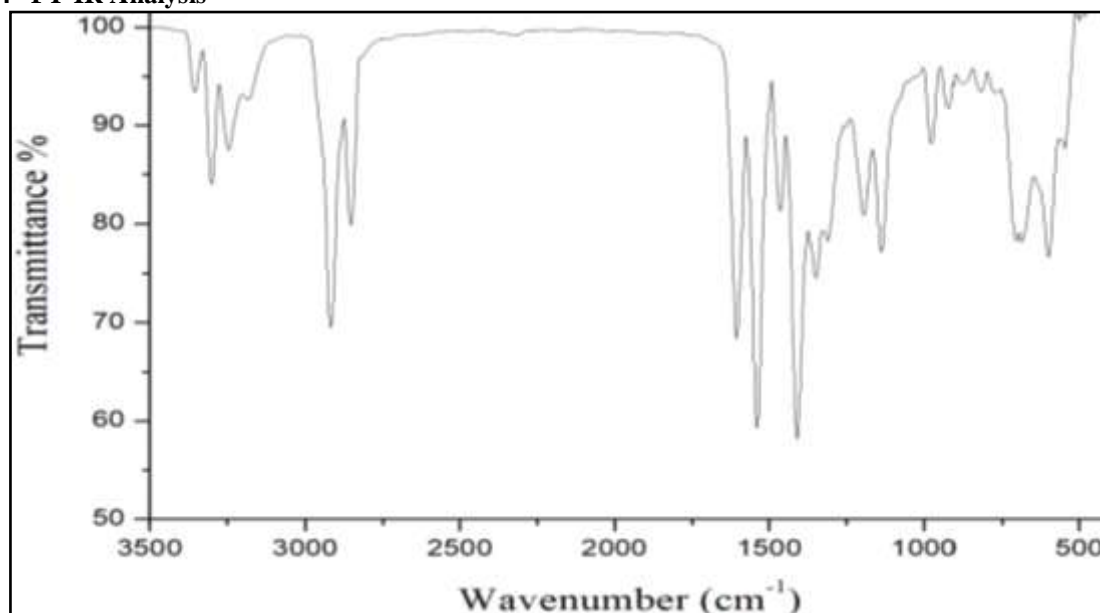


Figure 3 FT-IR spectrum of Zn(Lau).1.5N₂H₄

Table 3 FT-IR analysis Co-Zn(Lau).1.5N₂H₄

Precursor	ν_{O-H} cm ⁻¹	ν_{N-H} cm ⁻¹	ν_{asym} (COO ⁻) cm ⁻¹	ν_{sym} (COO ⁻) cm ⁻¹	$\Delta\nu$ cm ⁻¹	ν_{N-N} cm ⁻¹
Co-Zn(Lau).1.5N ₂ H ₄	---	3244- 3354	1606 1539	1463 1409	143 130	975



The FT-IR spectra of the precursor shown in Figure 3 have three bands in the region 3244–3354 cm⁻¹, which are characteristic of N–H stretching frequencies. The N–N stretching frequency is observed at 975 cm⁻¹ which confirms the presence of hydrazine as bidentate bridging ligand [16]. The asymmetric stretching frequencies of the carboxylate group in the precursor are observed at 1606 cm⁻¹ and 1539cm⁻¹.The symmetric stretching frequencies of the carboxylate group in the precursor are observed at 1463 cm⁻¹ and 1409 cm⁻¹.The (asym–sym) separation of 143 cm⁻¹ and 130 cm⁻¹ indicate the bidentate bridging nature of carboxylate group. These results support the

formation of Cobalt doped Zn(lau).1.5N₂H₄ precursor. The infrared spectra analysis data are given in Table 3.

3.2 Characterization of the synthesized Co-ZnO NPs

3.2.1 FT-IR analysis

From the FT-IR spectra in Figure 4, we observe peak only at 451 cm⁻¹, for Co-ZnO NPs which corresponds to the metal-oxygen stretching vibration. Peaks corresponding to organic species and hydrazine are completely removed. This confirms that after thermal decomposition only the metal oxide exist [17].

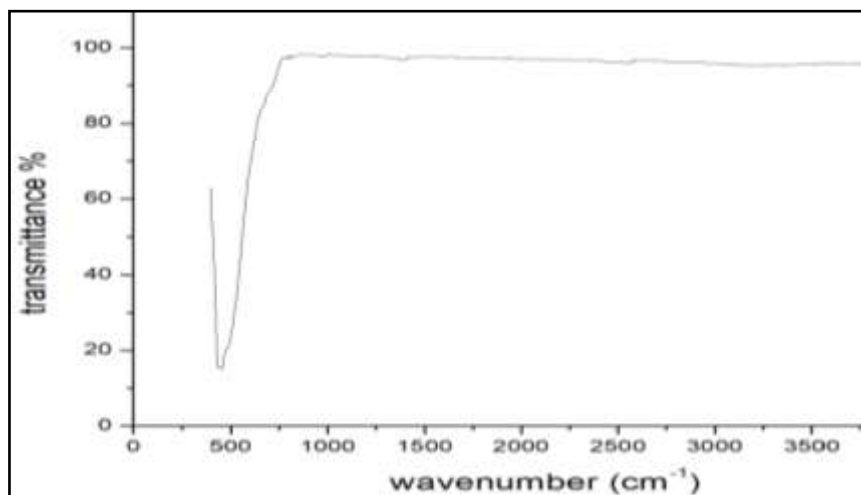


Figure 4 FT-IR spectrum of Co-ZnO NPs

3.2.2 Energy Dispersive X-ray Analysis (EDX)

The EDX analysis shown in Figure 5 shows the presence of metals in Co-ZnO NPs and it

is clear that there is incorporation of cobalt and no other elemental impurities present in the synthesized nanostructures.

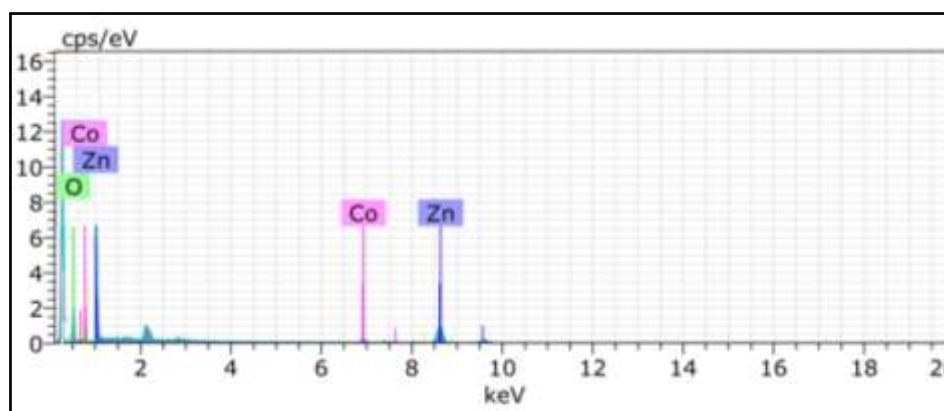


Figure 5 EDS of Co-ZnO NPs

3.2.3 ICP-AES analysis

The composition of Co-ZnO NPs were analysed using ICP-AES and given in Table 4. The

estimated values of metals agreed with the expected values. This result confirms the absence of loss of metals during thermal decomposition

Table 4 Composition of Co-ZnO NPs obtained from ICP-AES analysis

Nanoparticles	Zn%		Co%	
	Obs	cal	Obs	cal
Co- ZnO	81.07	80.37	4.39	5.28

3.2.4 X-ray diffraction pattern (XRD)

As shown in figure 6 the X-ray diffraction measurements of the Co-doped ZnO nanoparticles showed wurtzite structures. All the peaks are sharp, properly indexed and well in agreement with that of standard datasheet (JCPDS-036-1451) corresponding to the hexagonal wurtzite. The peaks at 31.74°, 34.45°, 36.27°, 47.6°, 56.63°, 62.89°, 66.31°, 68.11°, 69.04°, 72.64°, 76.99° can respectively be indexed to (100), (002), (101), (102), (110), (103), (200), (112), (201), (004) and (202) planes of hexagonal wurtzite ZnO structure. No additional intensity peak of metallic Co or

related compounds is detected under the sensitivity of an X-ray diffractometer, which rules out the possibility of any secondary phase. Thus cobalt is well doped in the ZnO lattice. The average crystallite size is calculated using Debye-Scherrer formula, $D = K\lambda / \beta \cos\theta$, where D is crystallite size (nm), θ is Bragg diffraction angle, λ is the source wavelength (1.54) and β is the width of the XRD peak at half maximum height. The calculated average crystallite size of Co-ZnO NPs is found to be around 13.45 nm. The sharp peaks indicate the high crystalline nature of synthesized nanoparticle.

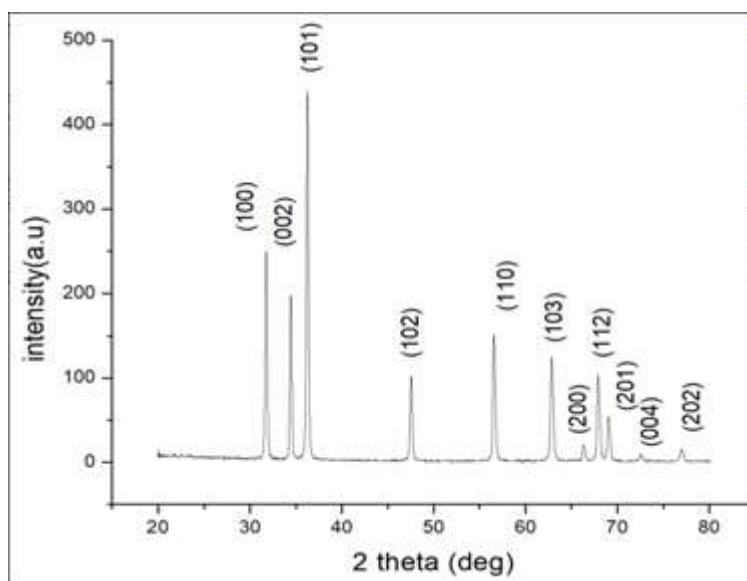


Figure 6 X-ray diffraction pattern of Co-ZnO nanoparticles

3.2.5 SEM and TEM analysis

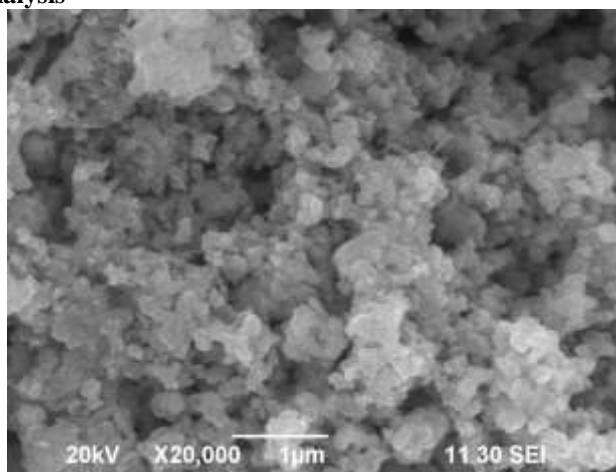


Figure 7 SEM image of Co-ZnO NPs

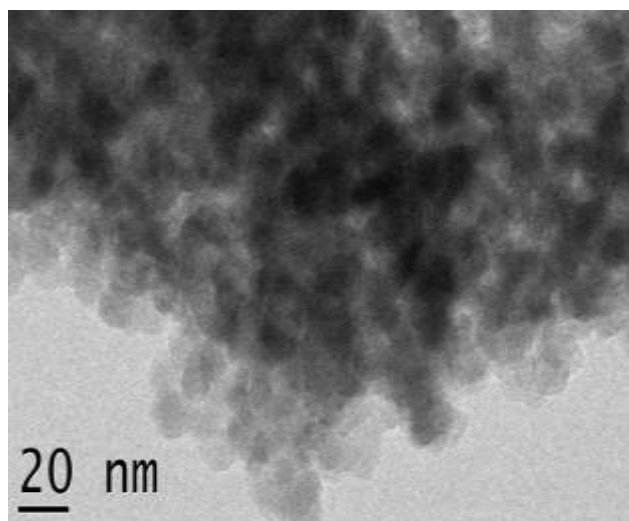


Figure 8 TEM image of Co-ZnO NPs

The SEM image shows the external morphology of nanoparticles. From Figure 7 Co-ZnO NPs exhibit that, the majority of particles are of polygonal shape. It is clear that the small particles are aggregated or overlapped to each other. From TEM micrographs in Figure 8 the average diameter is calculated, from measuring over 100 particles in random fields of TEM view. The average TEM diameter of Co-ZnO NPs is between 10 to 20 nm.

3.2.6 UV-VISIBLE-NIR absorption spectra

Absorption spectra for Co-ZnO NPs present a significant absorbance in the visible region along with a broad absorption in UV region as shown in Figure 9. With Co doping, the three characteristic absorption peaks corresponds to the d-d transition of Co^{2+} ions has been observed (563 nm, 610 nm and 657 nm) in the visible region. This confirms that most of the Co^{2+} occupies the Zn^{2+} sites in ZnO lattice, rather than precipitating as cobalt oxide (CoO) or Co metal [15].

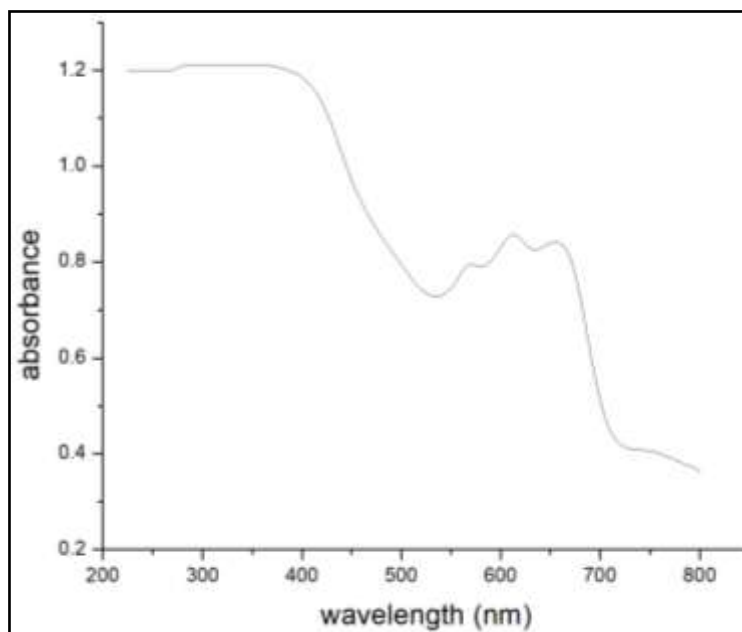


Figure 9 UV-VISIBLE-NIR absorption spectrum of Co-ZnO NPs

3.3 In Vitro Cytotoxicity of Co-ZnO NPs

The synthesized Co-ZnO NPs were tested for their potent cytotoxic activity against human breast cancer cells (MCF-7) and human embryonic kidney normal cells (HEK- 293) using MTT assay. MCF-7 and HEK- 293 cell viability were evaluated after 48 h exposure to Co-ZnO NPs of various concentrations ranging from (6.25µg/ml to 50µg/ml). The living cells, convert the MTT assay

to an insoluble purple formazan. The quantity of formazan (presumably directly proportional to the number of viable cells) is measured by recording changes in absorbance at 570 nm using micro plate reader. The % cell viability was determined using the following formula, % Cell viability = {Abs (sample)/Abs (control) x100} and shown in Figure 10.

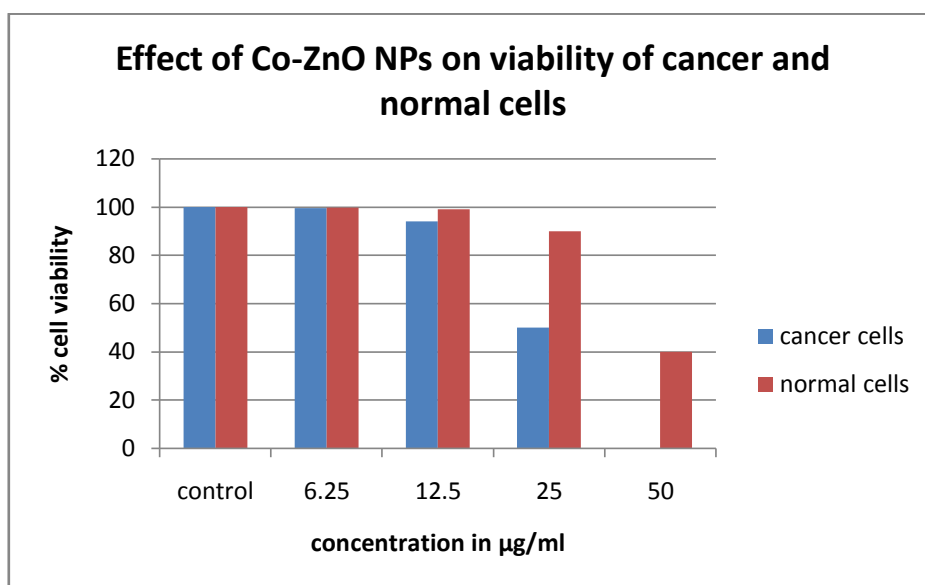


Figure 10 the percentage viability of MCF 7 cancer cell lines and HEK 293 normal cell lines using MTT assay after 48 h exposure to Co-ZnO NPs (6.25 to 50 µg/mL). Data represented are mean ± standard deviation of three identical experiments made in triplicate

Figure 10 show that Co-ZnO NPs induce cytotoxicity in a dose-dependent manner. In addition, the selected NPs show strong and differential cytotoxicity in cancer versus normal

cells. These nanoparticles are selectively toxic to cancer cells and at concentrations much lower than required for normal.

3.3.1 Evaluation of IC50 value

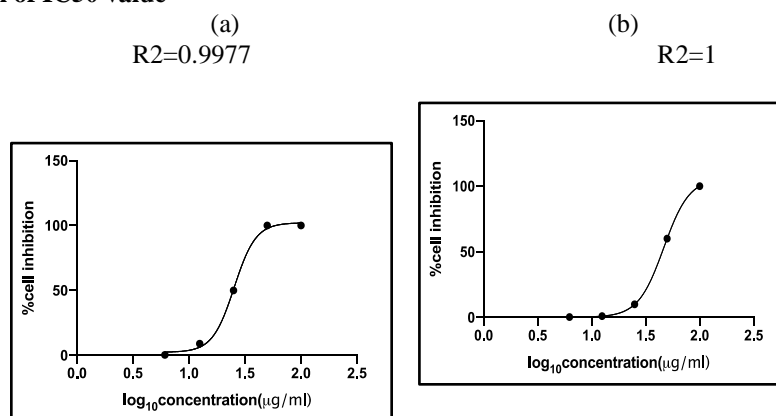


Figure 11 cytotoxicity of Co-ZnO against (a) cancer cell line (MCF7) IC50 value 25µg/ml and (b) normal kidney (HEK 293) cell line IC 50 value 46µg/ml.

Figure 11 shows the Non linear regression graph plotted between % Cell inhibition and Log concentration. IC₅₀ was determined using Graph Pad Prism software. Here we present novel findings that cancerous cells are markedly more susceptible (1.84 times) to Co-ZnO NPs mediated toxicity than their normal counterparts (the IC₅₀ value 25 μ g/ml for cancer cells and 46 μ g/ml for normal cells). At lower concentrations Co-ZnO NPs are less toxic to normal cells. Thus these Co-ZnO NPs can act as a potential candidate for developing anti-cancer therapeutics. ROS generation is proposed as one of the key cytotoxic mechanism for ZnO NPs. The mechanism of Co-ZnO NPs cytotoxic effects on cell death is not fully understood.

3.3.2 ROS generation

As normal cells and cancerous cells provide different atmosphere, the synthesized CoZnO NPs may generate different level of ROS and have different cytotoxicity towards cancer and normal cells. We have determined the ROS generation by the synthesized NPs to confirm that the selectivity toxicity is due to of ROS generation, Figure 12 show the of ROS generation in both in normal cells and cancer cells. It is seen that ROS generation and cell damage are very closely related. Hence, the differential cytotoxicity of CoZnO NPs may be because of different levels of ROS generation. Oxygen vacancies present in the crystal structure of transition metal doped metal oxides nanostructures produces more level of ROS generation.

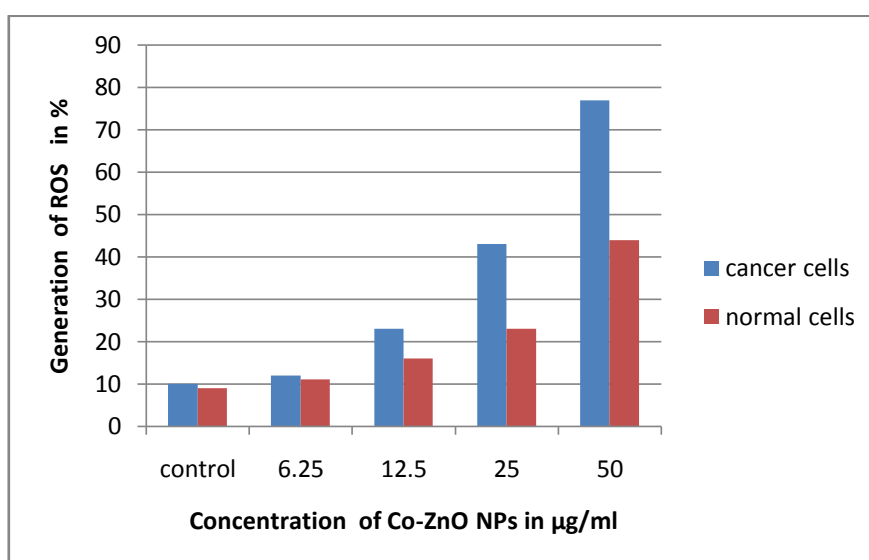


Figure 12 Detection of ROS production by Co-ZnO nanoparticles (6.25–50 μ g/ml) in MCF-7 cancer cells and (HEK 293) normal cells. Data represented are mean \pm standard deviation of three identical experiments made in triplicate

IV. CONCLUSION

The synthesis of Co-ZnO NPs with crystalline and wurtzite like structure were successfully achieved by a simple thermal decomposition. The synthesized cobalt doped ZnO NPs cytotoxicity against human breast cancer cells (MCF-7) and its cytotoxicity against human embryonic kidney normal cells (HEK 293) in vitro were studied. We present the finding that cancerous cells are markedly susceptible to cobalt doped NPs than normal cells. As the NPs have strong absorption in the visible region, they can produce reactive oxygen species on visible light irradiation.

Thus inherent selective cytotoxicity of the nanoparticles against cancer cells can be improved by irradiating with visible light. Thus these NPs are promising material for cancer therapy. Further research on anticancer activity of Co-ZnO NPs in different types of cancer cells is warranted. We have to do more work to develop practical applications of these nanoparticles.

Acknowledgements The authors are thankful to Kongunadu Arts and Science College, Coimbatore, for providing facilities. We acknowledge the provision of necessary facilities by SAIF Cochin,

IIT Madras, Karunya University, Coimbatore and
KMCH College of Pharmacy Coimbatore.

REFERENCE

- [1]. R. Augustine, A.P. Mathew, & A. Sosnik, *Applied Materials Today*, 7, 91–103, 2017.
- [2]. J. W. Rasmussen, E. Martinez, P. Louka and D.G. Wingett, *Expert Opinion On Drug Delivery* 7, 1063-1077, 2010.
- [3]. C. Hanley, J. Layne, A. Punnoose, K. M Reddy, I. Coombs, A. Coombs, K. eris and D. Wingett, *Nanotechnology* 19, 295103, 2008.
- [4]. C.T. Ng, L.Q. Yong, M. P. Hande, C. N. Ong, L. E. Yu, B. H. Bay and G. H. Baeg, *International Journal of Nanomedicine* 12, 1621-1637, 2017.
- [5]. G. H. He, H. Zhou, H. Shen, Y. J. Lu, H. Q. Wang, J. C. Zheng, B. H. Li, C. X. Shan and D. Z. Shen, *Appl. Surf. Sci.*, 412, 554, 2017.
- [6]. P. Sivakumar, M. Lee, Y. S. Kim and M. S. Shim, *Journal of Materials Chemistry B* *Journal of Materials Chemistry B* 6, 4852-4871, 2018.
- [7]. A. A. Jacob, L. Balakrishnan, K. Shambavi, & Z. C. Alex, *RSC Advances*, 7(63), 39657–39665, 2017.
- [8]. S. Kuriakose, B. Satpati, & S. Mohapatra, *Physical Chemistry Chemical Physics*, 16(25), 12741, 2014.
- [9]. A. Chanda, S. Gupta, M. Vasundhara, S. R. Joshi, G. R. Mutta, & J. Singh, *RSC Advances*, 7(80), 50527–50536, 2017.
- [10]. I. A. Sarsari, H. Salamati, P. Kameli, P & F. S. Razavi, 24(8), 2293–2298, 2011.
- [11]. Vasuki, K., & Manimekalai, R. *Heliyon*, 5(11), e02729, 2019.
- [12]. Anjuthaprabha, N., & Manimekalai, R. *Journal of Coordination Chemistry*, 1–13, 2019.
- [13]. Gawas, S. G., & Verenkar, V. M. *S. Thermochimica Acta* 605: 16–21. 2015.
- [14]. R. Selvakumar, S. J. Geib, T. Premkumar, S. Vairam and S. Govindarajan *New J. Chem.*, 40, 257-264. 2016.
- [15]. I. Vogel, “A Textbook of Quantitative Inorganic Analysis”, 4th Ed., Longman, UK, 1985.
- [16]. A. Braibanti, F. Dallevale, M. A. Pellinghelli and E. Leopardi, *Inorg. Chem.*, 7, 1430-1433, 1968.
- [17]. T. Thangeeswari, A. T. George & A. Arun Kumar, *Indian Journal of Science and Technology*, 9(1), 2016.
- [18]. M. Shatnawi, A. M. Alsmadi, I. Bsoul, B. Salameh, G. A. Alna'wash, F. Al-Dweri and F. El Akkad, *J. Alloys Compd.*, 655, 244, 2016.